Impact of Microheterogeneity on Upscaling Reactive Transport in Geothermal Energy

Erfani, Hamidreza; Joekar-Niasar, Vahid; Farajzadeh, Rouhi

DOI
10.1021/acsearthspacechem.9b00056

Publication date
2019

Document Version
Final published version

Published in
ACS Earth and Space Chemistry

ACS EARTH AND SPACE CHEMISTRY

Article

Cite This: ACS Earth Space Chem. 2019, 3, 2045−2057

http://pubs.acs.org/journal/aesccq

Impact of Microheterogeneity on Upscaling Reactive Transport in Geothermal Energy

Hamidreza Erfani,[†] Vahid Joekar-Niasar,*[,†] and Rouhi Farajzadeh[‡]

[†]Department of Chemical Engineering and Analytical Science, University of Manchester, Oxford Road, Manchester M13 9PL, U.K.

[‡]Faculty of Civil Engineering and Geosciences, Delft University of Technology, 2628CN Delft, The Netherlands

Supporting Information

ABSTRACT: Reaction rates for different minerals are usually measured in ideal conditions in batch experiments, where the impact of pore morphology and hydrodynamics have been fully neglected. Such reaction rates are used at continuum-scale (Darcy-scale) models without the impact of pore structure on upscaled reaction rates under flow conditions. Therefore, to address the gap from batch experiments to upscaled reaction rates in continuum-scale models, a pore-network model coupled with geochemical modeling has been developed. As a case study, we simulate the geochemical reactions of geothermal energy storage/recovery in sandstone rocks by coupling PhreeqcRM (a geochemistry model) with a pore-network model. The main purpose is to delineate the impact of pore morphology and dynamic conditions on upscaling of reaction rates using the surface-weighted and volume-weighted averaging. The results show that the kaolinite reaction rate in porous media highly depends on both the flow rate and spatial distribution of reactive pores. We evaluate the impact of correlation between the reactive pores and pore size distribution on upscaled reaction rates. Results indicate that if reactive pores do not belong to the main flow path, then upscaling the geochemical reactions based on the continuum-scale or batch experiments would be erroneous. In such a scenario, the discrepancy between volume-averaged and surface-weighted average reaction rates are highlighted. Moreover, increasing the injection flow rate results in lower average concentration of different species in the effluent, while it results in higher reaction rates in porous media. This research provides insights into the complex aspects of flow-based reaction rates versus the batch reaction rates. That has a significant impact on continuum-scale modeling of reactive transport for applications such as geothermal energy and enhanced oil recovery.

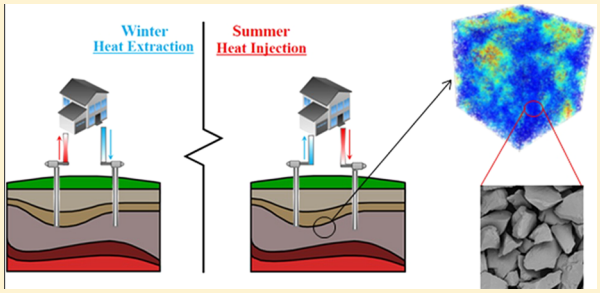

KEYWORDS: *reactive transport, PHREEQC, geochemistry, geothermal energy, pore-network modeling*

INTRODUCTION

Modeling reactive transport in the subsurface is essential for better understanding of many applications ranging from enhanced oil recovery (EOR) such as alkaline surfactant polymer (ASP) flooding,[1,2] low-salinity waterflooding,[3−8] and chemical injection[9,10] to underground CO_2 storage,[11−15] geothermal energy storage/recovery,[16−19] groundwater and soil contamination,[20−22] and nuclear waste disposal.[23,24] Our understanding of the reactive transport process is highly dependent on modeling across different physical scales because of multiscale aspects of flow and transport in porous media as well as difficulty in in situ sampling/measurements of the geochemical reactions.

Geochemical reaction rate constants are mostly measured in batch experiments in the laboratory that can be significantly different from the in situ or flow-based reaction rates. However, the reactive transport models at the Darcy scale mostly use batch mineral reaction rates to calculate the progress of reactions in natural porous media, which may lead to erroneous results due to the discrepancy in physical scales and hydrodynamic conditions.[25−27] Also, natural sedimentary rocks (carbonate and sandstone) are usually composed of different minerals, with considerably different reaction rates (up to 10 orders of magnitude variation).[28] For example, sandstone is mostly composed of quartz or feldspar and different clay minerals with highly variable clay content.[29] Reaction rates of clay minerals can be highly variable (2−8 orders of magnitude difference) at the same condition, but usually, they are larger than that of quartz.[28,30] It is worth mentioning that minerals may have different spatial distribution patterns in natural sedimentary rocks depending on source rock composition, sedimentation, and diagenesis processes.[31]

Pore-scale modeling is an alternative to the Darcy-scale modeling, which incorporates the detailed pore morphology. Many researchers have studied reactive transport at the pore scale, mostly using pore-network modeling,[32−40] lattice Boltzmann,[35−37] and computational fluid dynamics.[38−40] While many of the utilized pore networks were structured lattices, an unstructured pore-network model is used in this

Received: March 15, 2019
Revised: July 14, 2019
Accepted: July 29, 2019
Published: July 29, 2019

DOI: 10.1021/acsearthspacechem.9b00056
ACS Earth Space Chem. 2019, 3, 2045−2057

study to be a better representative of sandstone. Moreover, there has been very limited investigation on the impact of micro-heterogeneity of pore size distribution and spatial distribution of mineralogy on the upscaled reaction rates.

Varloteaux et al.[34] compared pore-network modeling with a pore-scale model developed by Békri et al.,[41] combined with the level-set method. Oostrom et al.[42] performed four sets of solute transport experiments in the micromodel and used five pore-scale models and one continuum-scale model to simulate the experiments. It was concluded that the pore-network modeling is not only computationally efficient but also satisfactorily simulating the experiments.

Li et al.[43] utilized pore-network modeling to study the applicability of averaged (upscaled) reaction rates in the CO_2 injection process with the focus on sandstone containing anorthite (Ca-rich feldspar) and kaolinite. They used a regular lattice of 9000 pores with a constant coordination number of 4 as the network structure and simulated the flow of highly acidic water through rock under steady-state single-phase condition, relevant to CO_2 storage and sequestration. They also studied the effect of reactive mineral spatial distribution,[44] reactive cluster size, and hydrodynamic condition[45] on upscaled reaction rates and concluded that, due to the pore-scale heterogeneity and local variation of reaction rates, upscaling geochemical reaction can be associated with large errors and significant scaling effects.

Ameri et al.[46] coupled PHREEQC with a pore network to simulate carbonate acidizing. Comparison of simulation results with micro-computed tomography experimental data provided satisfactory match in terms of permeability evolution pattern. Qin et al.[47] studied microbial-induced calcium carbonate precipitation (MICP) in a 2D network. They showed that there was a higher possibility of biofilm generation in pore throats rather than pore bodies due to greater specific area in throats. The provided results confirmed that the final distribution of calcium carbonate depended on the biofilm distribution in the network.

Al-Khulaifi et al.[48] showed experimentally the transient behavior and pore-scale heterogeneity of effective reaction rate using X-ray tomography, coupled with mass spectrometry of the effluent in a composite (Silurian dolomite and Ketton limestone) millimeter-scale core. Holmslykke et al.[49] performed core-flooding experiments to study the effect of temperature (up to 150 °C) and flow rate on reactive transport in porous media with applications to seasonal aquifer heat storage in Gassum sandstone formation in the Stenlille area. They used PHREEQC[50] software to model the experiments and showed the possible precipitation of kaolinite and the sharp increase in both iron and silicon concentrations in effluent water above 100 °C.

In this work, we aim to understand what factors influence the Darcy-scale reaction rates. Experimental approaches cannot provide in situ pore-scale reaction rates and distributions of different species in the sample. However, the pore-scale simulation techniques can give a valuable capability to simulate pore-scale reactions coupled with flow and transport and can be used as a tool to understand the impact of spatial distribution of pore sizes and mineralogy on the upscaled reaction rates. We use pore-network modeling coupled with PhreeqcRM,[51,52] a geochemistry module, to model reactions in geothermal energy extraction[53,54] and aquifer thermal energy storage (ATES)[49,55] in sandstones in moderate pH values. The major objective of this work is to investigate the following:

1. Impacts of spatial distribution of reactive pores and pore size correlation on the average reaction rates calculated using surface-weighted averaging versus volume-weighted averaging.
2. The effect of different averaging schemes on averaged reaction rates of different minerals in sandstones that give insight into potential uncertainties for parameterization of geochemical modeling at the Darcy scale.

To achieve these objectives, we have developed a coupled PHREEQC pore-network model that can be used for simulation of any geochemical reactions at single-phase flow condition. This coupled model is a versatile and flexible pore-scale model that can be used and adapted to different subsurface reactive transport modeling applications.

In the remainder of the paper, first, the theoretical backgrounds of reaction equilibrium constants, diffusion coefficients, and experimental reaction rates are presented. Then, the formulation of the pore-network modeling will be provided. Next, network generation and pore-network simulation processes, along with the methods for averaging reaction rates, are discussed. In the Results and Discussion section, cross-correlated reactive networks are generated, and then the effects of spatial distribution of the reactive pores, injection flow rate, and network structure on the averaged reaction rates are discussed. In the end, concluding remarks and implications of the results to ATES and geothermal energy extraction, learned from pore-scale modeling, will be discussed.

THEORETICAL BACKGROUND

Geochemistry of Sandstone Rocks for ATES. The geochemistry of sandstone rocks in ATES is highly dependent on the operating temperature, rock mineralogy, and injection fluid. We assumed that the rock was composed of quartz (SiO_2), kaolinite ($Al_2Si_2O_5(OH)_4$), albite ($NaAlSi_3O_8$), anorthite ($CaAl_2Si_2O_8$), and siderite ($FeCO_3$) minerals to represent a realistic sandstone mineral assemblage based on a typical geothermal site in Denmark, named the Gassum formation.[49] The network was composed of pore bodies (spheres) and pore throats (cylinders), which both had a volume and surface. Pore units (i.e., each pore unit comprises a pore body and half-length of the connecting pore throats) were either reactive or nonreactive. Kinetic and local equilibrium reactions are the two common reactions to model rock and fluid interactions in reactive transport modeling. The local equilibrium approach (LEA) is recommended for relatively fast reactions, where transport is the limiting factor for the process such as water/calcite interaction. The kinetic approach is used for the systems where the process needs a considerable time to reach the equilibrium condition. Quartz, kaolinite, siderite, anorthite, and albite reactions were considered as kinetic reactions. Steady-state single-phase flow was assigned to each simulation case. The injection fluid was assumed to be acidic (pH ≈ 5.0) relevant to ATES.[49] The PhreeqcRM geochemical module was coupled with the transport model to handle the kinetic and equilibrium geochemical reactions.

Geochemical Reaction Rates. The reaction rate law or the rate equation is a function that describes mineral (phase) dissolution/precipitation rate with the general form of

$$r = k \prod_s \{s\}^{n_s} (1 - \Omega^m) \quad (1)$$

DOI: 10.1021/acsearthspacechem.9b00056
ACS Earth Space Chem. 2019, 3, 2045−2057

where r is the reaction rate (mol/m^2 s), k is the reaction-rate constant (mol/m^2 s), s is the chemical species with a catalytic or prohibitive effect on the phase reaction, $\{s\}$ denotes the activity of species s, n_s is a constant describing the degree of rate dependence on species s, Ω is the phase saturation ratio, and m is a constant that describes the dependence of rate on the saturation state.

Saturation ratio is an indication of how far the reaction is from the equilibrium state and is equal to the ratio of the ionic activity product (IAP) to the reaction equilibrium constant (K_{eq}, which is discussed in the Supporting Information in detail). Since the values of Ω cover orders of magnitude, the saturation index (SI = log Ω) is used to quantify the saturation state. If $\Omega < 1$ (SI < 0), then the net reaction is in forward direction, meaning that more solid can dissolve in the aqueous phase. Conversely, if $\Omega > 1$ (SI > 0), then the aqueous phase is supersaturated and the net reaction is in the precipitation direction. If $\Omega = 1$ (SI = 0), then the system is at equilibrium. As an example, the kaolinite dissolution reaction is as follows

$$Al_2Si_2O_5(OH)_4 + 6H^+ \rightleftharpoons H_2O + 2Al^{3+} + 2H_4SiO_4 \quad (2)$$

Mineral dissolution and precipitation reactions are generally described by different mechanisms, each of them being catalyzed by different chemical species, for instance, H^+, OH^-, and H_2O. The rate law for each mechanism has the general form of eq 1, and the total reaction rate is the summation of all involving mechanisms. So, for kaolinite, the reaction rate equation (r_K) reads

$$r_K = (k_H\{H^+\}^{n_1} + k_{H_2O} + k_{OH}\{OH^-\}^{n_2})(1 - \Omega_K^m) \quad (3)$$

Also, the expression for the saturation ratio of kaolinite (Ω_K) is as follows

$$\Omega_K = \frac{\{Al^{3+}\}^2\{H_4SiO_4\}^2}{\{H^+\}^6 K_{eq,K}} \quad (4)$$

It can be inferred from eq 3 that, under acidic conditions, the first term (H^+ activity) determines the rate of dissolution of kaolinite and the other terms can be neglected; under basic conditions, the third term (OH^- activity) is more important than the other two terms. Also, the second term is more important under basic conditions in comparison with the acidic condition. As ATES is performed at high temperatures and the system is nonisothermal, it is important to consider the effect of temperature on the reaction rate constants. The temperature dependency of the reaction rate constant is expressed by the Arrhenius equation. Eventually, one can write the rate (mol/s) for the reactive surface of $\mathcal{A}$ (m^2) as

$$r = \mathcal{A}\left[\begin{array}{c} k_{298.15}^{acid} \times e^{[-E_a^{acid}/R(\frac{1}{T}-\frac{1}{298.15})]} \times \{H^+\}^{n_1} + \\ k_{298.15}^{neutral} \times e^{[-E_a^{neutral}/R(\frac{1}{T}-\frac{1}{298.15})]} + \\ k_{298.15}^{base} \times e^{[-E_a^{base}/R(\frac{1}{T}-\frac{1}{298.15})]} \times \{OH^-\}^{n_2} + \end{array}\right] (1 - \Omega^m) \quad (5)$$

Reaction rate coefficients for different kinetic reactions of this study are presented in Table S-3.

PORE-NETWORK GENERATIONS AND SIMULATION

To investigate the geochemical reactions for ATES at the pore scale, the pore morphology should be introduced. Results of the network were averaged over the network to calculate the Darcy-scale values. Laminar flow was assumed at pore throats, and pore bodies were assumed to be fully mixed, that is, uniform concentration in each pore element.[56] Each pore body and half-length of the connecting pore throats are assumed as a pore unit, and the corresponding surface area is assumed as the reaction surface area for each pore unit.

Network Structure. The first step in the pore-network modeling is to construct a network of connected pores and throats. In this study, we have used the same methodology developed by Leng[57] and further improved by Babaei and Joekar-Niasar[58] to construct unstructured anisotropic networks with different correlation lengths. To study the effect of the network structure and correlation length, we have used two different networks, with correlation lengths of 1 μm (hereafter named random/uncorrelated network) and 20 μm (named correlated network). Both networks have the same size, topology, coordination number, and pore and throat size distribution, and the only different factor is the spatial distribution of the pore sizes. Both networks have 56,000 pore bodies, and the size is 4.6 × 4.6 × 4.6 mm^3. The 3D representations of both networks, pore size, and coordination number distributions are shown in Figure 1.

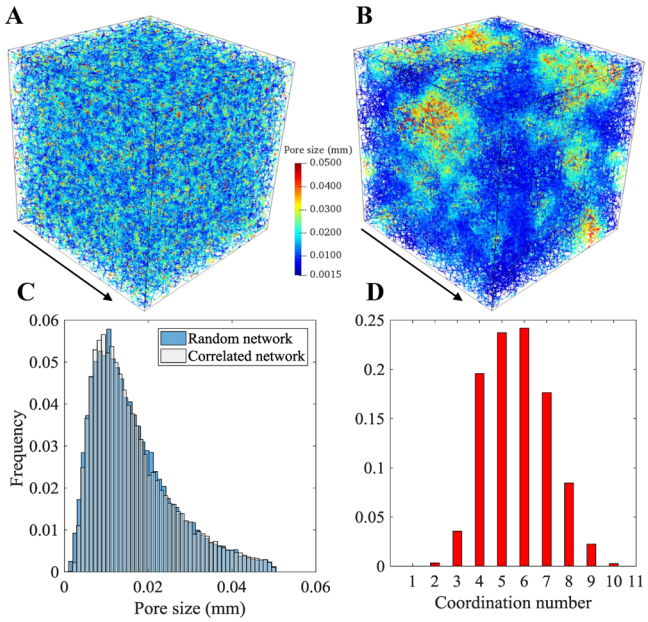

Figure 1. 3D visualizations of (A) uncorrelated (random) and (B) correlated networks; (C) pore size and (D) coordination number distributions. Arrows show the flow direction. (Note that all pores are shown with the same size for the sake of visualization.)

Steady-State Single-Phase Flow Modeling. The system is assumed to be at steady-state condition. The mass conservation for different species considering sink/source terms due to the kinetic reactions is solved over the steady-state flow field. To determine the steady-state flow field over the network, fixed fluid pressures are imposed at the inlet and outlet boundaries ($P_{inlet} > P_{outlet}$) in the flow direction with no-flow boundary conditions in other two orthogonal planes. In the

DOI: 10.1021/acsearthspacechem.9b00056
ACS Earth Space Chem. 2019, 3, 2045−2057

pore-network modeling, the computational nodes are pore bodies, so mass balance is solved in all pore bodies (eq 6); the flow rate between two connecting pore bodies is proportional to the differential pressure between the connecting pore bodies, multiplied by the hydraulic conductivity, which is calculated based on the Hagen−Poiseuille flow equation.

$$\sum_{j=1}^{np} Q_{ij} = \sum_{j=1}^{np} \frac{\pi {d_{ij}}^4}{128\mu l_{ij}}(P_i - P_j) = 0 \tag{6}$$

where Q_{ij} (mm^3/s) is the flow rate between pore bodies i and j; P_i and P_j (Pa) are fluid pressures in pores i and j, considering that the flow is from pore i to pore j; d_{ij} and l_{ij} (mm) denote the diameter and length of the connecting throat, respectively; and μ (Pa s) is the fluid viscosity. Writing eq 6 for all pore units results in a linear system of equations as ($\underline{\underline{K}}P = \underline{B}$), where $\underline{\underline{K}}$ is a square sparse coefficient matrix of size $np \times np$, P is the unknown pressure field vector, and $\underline{B}$ is the right-hand (known) vector. This system of algebraic equation is solved using the biconjugate gradient squared method with diagonal scaling, and the pressure field is calculated over the network by means of which one can calculate the steady-state velocity field.

Reactive Transport Modeling. In each pore, the concentration of each species changes due to transport (advection and diffusion) and chemical reactions. To solve the coupled flow and reactions, a sequential noniterative approach (SNIA) is used.[1,52,59] In this scheme, fluid flow and chemical reactions are solved separately and sequentially, and it is assumed that, during transport time step, the aqueous-phase chemistry does not change. Then, after calculation of the transport equations, the chemical composition of the aqueous phase is updated for all reactive pores to be used in the next time step. Solving the geochemical reaction in the assigned time step is handled by the PhreeqcRM geochemical module. Detailed numerical schemes for solving ordinary differential equations corresponding to each geochemical reaction/aqueous-phase reactions can be found in PHREEQC documentation.[50] The SNIA approach is accurate if the time step is small enough in comparison to the rate of the reaction. In addition, the changes of the component concentrations due to the chemical reactions must be smaller than the concentration change due to transport. SNIA is computationally less expensive in comparison to the fully implicit method, but it needs smaller time steps to guarantee numerical stability and acceptable accuracy.[60,61] In this study, the time-step calculation is based on the concept of residence time. Given that multiple species are present, each component has its own residence time. We consider the shortest residence time of all species as the global time step. To calculate the residence time, rates of change for all species in all pore units were calculated, and then the residence time of all species in all pore units was calculated considering whether they were increasing or decreasing to reach the maximum or minimum concentration.

Transport equations are solved for each species separately, and then the mass balance equation for each pore unit is described as follows

$$V_i \frac{\mathrm{d}[c]_i}{\mathrm{d}t} = \underbrace{\sum_{j=1,Q_{ij}>0}^{n_{ct_i}} Q_{ij}[c]_i + \sum_{j=1,Q_{ij}<0}^{n_{ct_i}} Q_{ij}[c]_j}_{\text{Advection}} + \underbrace{\sum_{j=1}^{n_{ct_i}} D_{c,ij} a_{ij} \frac{[c]_i - [c]_j}{l_{ij}}}_{\text{Diffusion}} + \underbrace{S_{i,c}}_{\text{Reaction}} \tag{7}$$

Equation 7 is written for component c in the pore body number i. n_{ct_i} denotes the number of connecting throats to the pore body i. $[c]$ (mol/L) denotes the concentration of component c. Q_{ij} is the flow rate entering pore body i from connecting pore body j: if $Q_{ij} < 0$, the flow is entering the pore body i, and conversely, if $Q_{ij} > 0$, the flow is leaving the pore body i. $D_{c,ij}$ (mm^2/s) is the effective dispersion coefficient for component c including the Taylor−Aris dispersion, a_{ij} (mm^2) is the cross-sectional area of the connecting throat, and l_{ij} is the throat length. $S_{i,c}$ (mol/s) is the source/sink term for component c due to kinetic reactions in the pore body i, which is handled by PhreeqcRM. For example, for a pore unit, the aluminum (Al) sink/source term is as follows

$$S_{i,[\mathrm{Al}]_T} = 2 \times r_{i,\mathrm{K}} \mathcal{A}_{\mathrm{K}} + r_{i,\mathrm{A}} \mathcal{A}_{\mathrm{A}} + 2 \times r_{i,\mathrm{An}} \mathcal{A}_{\mathrm{An}} \tag{8}$$

where $\mathcal{A}_{\mathrm{K}}$, $\mathcal{A}_{\mathrm{A}}$, and $\mathcal{A}_{\mathrm{An}}$ are the reactive areas of kaolinite, albite, and anorthite, respectively. To calculate the species concentration of different components through all pore units of the network, eq 7 must be solved for all pore bodies over all components.

Coupled Geochemical Reactive Pore-Network Model. First, the steady-state solution of flow was solved, and the velocity field was obtained over the network. The composition of injection water at the inlet was kept constant for all time steps (fixed pH and concentration of the chemical components). Based on the velocity (advection) and diffusion of each species, the time step was set based on the smallest residence time in the pore units, considering all locally increasing or decreasing concentrations. After calculating the concentration change due to advection and diffusion, the aqueous phase chemical composition was fed into the PhreeqcRM module (in all reactive pores), the equilibrium and kinetic reactions were simulated for the time step, and then the aqueous-phase composition was updated as the output of the PhreeqcRM module. The flowchart of the calculation steps is presented in Figure S-1.

Averaged Reaction Rates. Two different averaging schemes were used to calculate the average network-scale reaction rates from the pore-scale simulation results. Surface-weighted average reaction rate for a continuum-scale domain is defined based on the mass change rate due to reaction at every reactive surface. As an example, for kaolinite, one can write

$$R_{\mathrm{S,K}} = \frac{\sum_{i=1}^{np} \mathcal{A}_{\mathrm{K},i} r_{\mathrm{K},i}}{\sum_{i=1}^{np} \mathcal{A}_{\mathrm{K},i}} \tag{9}$$

where np is the total number of pore units. As the reactive surface of kaolinite is zero in nonreactive pores, eq 9 results in a surface-weighted average of the local reaction rates. Analogous equations can also be defined for other reactive minerals. While eq 9 uses the distribution of the concentrations in the porous medium, one must define a reaction rate weighted by the volumes of the pore units ($\overline{R}$). This results in the resident average concentrations. As an example, during core-flooding experiments or in situ sampling (from a geothermal well as an

DOI: 10.1021/acsearthspacechem.9b00056
ACS Earth Space Chem. 2019, 3, 2045−2057

example), the produced fluid is a representative of a bigger domain rather than just reactive pores. The sampled fluid from a geothermal well is also representative of the average aquifer fluid properties. As an example, for kaolinite, we have

$$R_V = (k_H\{H^+\}^{n_1} + k_{H_2O} + k_{OH}\{OH^-\}^{n_2})(1 - \bar{\Omega}_K^m) \quad (10)$$

where $\{\bar{H}^+\}$ is the product of activity coefficient by the volume-averaged concentration of H^+ ion and can be calculated as follows

$$\bar{[H^+]} = \frac{\sum_{i=1}^{nn} V_i[H^+]_i}{\sum_{i=1}^{nn} V_i} \quad (11)$$

The overall saturation ratio of kaolinite ($\bar{\Omega}_K$) is calculated by eq 4 using the volume-averaged concentration of the involving species.

Simulation Scenarios. All simulations were conducted at a constant temperature of 100 °C. Initially, the in situ water was set to be at equilibrium with the rock minerals. Pore networks comprised two types of pores, reactive pores (consisting of reactive minerals) and nonreactive pores (in some studies, it was assumed that nonreactive quartz is present in these pores[43,44,62]). It was also assumed that mineral dissolution/precipitation did not change the composition of reactive minerals in the reactive pores and had no impact on the porosity and permeability of the sample. The fluid was assumed to be fully mixed in the pore bodies. The limiting factor was the reaction rate and not the mass transfer of the reactive species (mostly H^+) into the rock reactive surface. In the reactive pores, anorthite and quartz minerals each occupied 20% of the pore unit surface, albite and kaolinite each occupied 29.5% of the reactive surface, and the rest was occupied by siderite. As siderite is not widespread in sandstone rocks and is highly active, its amount was assumed to be low (1%).[49] Boundary condition for the network was the constant pressure at the inlet and outlet (which resulted in constant injection flow rate). The injection water at the inlet had fixed pH, chemical composition, and concentrations. Diffusion in the outflow pore throats was set to zero.

Since pore geochemistry might be correlated to pore sizes, three scenarios were considered. In the first case, 23.5% of the smallest pores (pores smaller than 23.5 percentile in the pore size probability distribution) were reactive; in the second case, 10% of the middle-sized pores (pores larger than 45 percentile and smaller than 55 percentile) were reactive; and in the third case, 2.6% of the largest pores (pores bigger than 97.4 percentile) were reactive. These cases were designed such that the total reactive surface area for all cases was similar. The pore size distribution, percentiles, and reactive pores are shown in Figure 2.

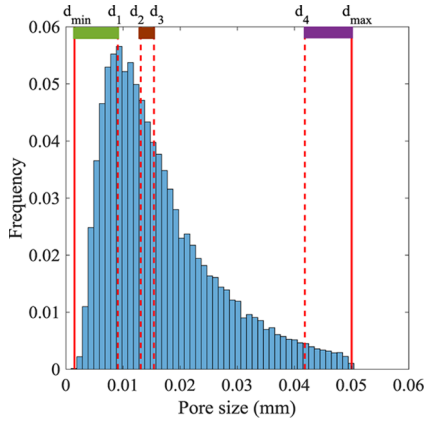

Figure 2. Probability distribution of pore size in the correlated network, d_{min} and d_{max}, are the minimum and maximum pore sizes and are equal to 0.0015 and 0.05 mm, respectively. d_1 to d_4 are 23.5, 45, 55, and 97.4 percentiles and are equal to 0.0091, 0.0131, 0.0154, and 0.0418 mm, respectively.

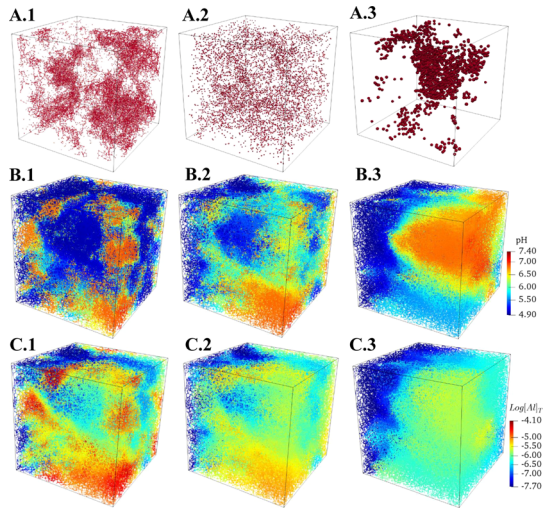

Figure 3. (A.1−A.3) Pattern of the reactive pores and the steady-state distribution of (B.1−B.3) pH and (C.1−C.3) $\log[Al]_T$ in the network for the cases in which the smallest (case 1), middle-sized (case 2), and largest (case 3) pores are reactive. (Note that pore-body sizes are scaled in A.1−A.3 but not scaled in B.1−C.3 visualizations.)

RESULTS AND DISCUSSION

Effect of Spatial Distribution of Reactive Pores on Averaged Geochemical Properties. In this section, we study the effect of spatial distribution of the reactive pores on different characteristics of the reactive transport in a sandstone rock sample, including average pH, average ion concentrations, surface-weighted average reaction rate, and associated discrepancy of the upscaled reaction rates. Figure 3 shows that the steady-state concentration and pH fields vary significantly for the three different presented cases. In case 1, in which the smallest pores are reactive, there is a clear distinction between the reactive and nonreactive pores, which has three reasons. First, the local flux is lower in the small pores as a significant amount of flow passes through the highly conductive pathways in the sample. Second, the ratio of the volume to the surface area is inversely proportional to the pore size, and as a result, the concentration change due to the reaction is higher in the small pores.[58] Last, in case 1, the reactive pores are present in the sample as clusters, which results in lower mixing with the nonreactive pores and higher saturation ratio of phases (SI ≥ 0).

By assigning the reactive pores to the large pores, the reactions take place in the main flow paths. Therefore, the reactive pores are flushed faster with injecting fluid than the case in which small pores are considered reactive. Consequently, the system is more heterogeneous in case 1, and the range of variation of the geochemical identities is wider. In all cases, the reactive pores act as H^+ consumption (which is associated with higher pH; see Figure 3B.1−B.3) and species production sites. This results in a lower pH and higher aluminum concentration in the reactive sites.

DOI: 10.1021/acsearthspacechem.9b00056
ACS Earth Space Chem. 2019, 3, 2045−2057

The steady-state distribution of pH in the network and the reactive pores are shown in Figure 4. For the sake of comparison,

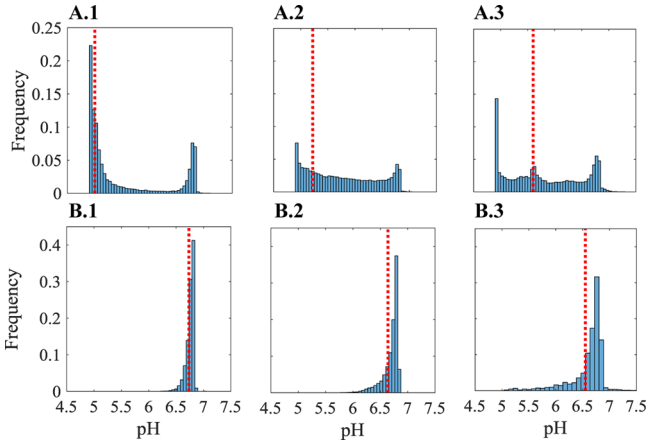

Figure 4. Steady-state pH distribution in (A.1−A.3) the network and (B.1−B.3) reactive pores for the cases in which the smallest (case 1), middle-sized (case 2), and largest (Case 3) pores are reactive. Average values are shown as dashed lines.

the average values of the aluminum concentration/pH in each case is also shown with a red dashed line. The transient behavior of the average pH for the network and the reactive pores as well as the average total aluminum concentrations ($[Al]_T$) are shown in Figure 5. In case 3, where the largest pores are reactive, the distribution is wider as the concentration of the reactive pores is affected by the neighboring pores. This is in agreement with findings of other studies.[44,45]

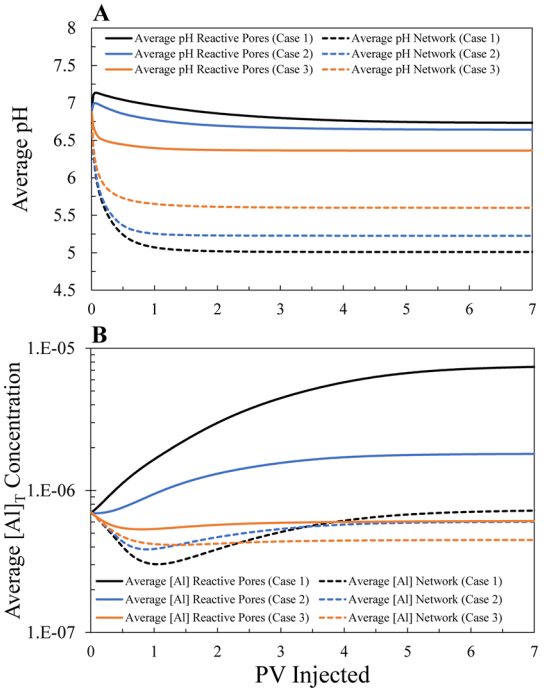

Figure 5. Effect of spatial distribution of the reactive pores on the transient behavior of (A) the average pH and (B) average aluminum concentration of the network and the reactive pores. (Note that injection water pH and aluminum concentration are 4.9 and 1.8×10^{-8} *m*, respectively.)

Figures 5A,B show the transient behavior of the average pH and aluminum concentration in the whole network and the reactive pores. Although the average pH of the reactive pores is higher in case 1, it has the lowest average pH over the network. The case in which the smallest pores are reactive (case 1) has a lower average pH in the reactive pores but a conversely higher average network pH. Based on Figure 5B, the average concentration of aluminum in the network first decreases and then increases as the injection continues. It happens because, initially, the system was in equilibrium with the rock minerals, which results in a high concentration of aluminum. Then, the system is washed with injecting fresh water at the early time of injection. Afterward, as a result of the kaolinite, albite, and anorthite reaction, the average concentration increases until it reaches a plateau.

The transient behavior of pH (Figure 5A) shows that, during all times, case 1 results in a higher pH. However, the early-time and steady-state trends of aluminum are different. At early times (from the start of injection up to 2 PV), case 3 shows the highest concentration, while case 1 has the lowest. However, this trend is completely opposite at the late times. This shows the nonlinear interactions between rock chemistry and flow pathways that cannot be illustrated without spatial mapping of pore morphology and spatial distribution of mineralogy.

Figure 6 shows the surface-weighted and volume-averaged reaction rates for kaolinite and albite for the three different cases. As can be seen, for kaolinite in case 1 (Figure 6A.1), the overall surface-weighted reaction rate is negative ($R_{S,\ \text{kaolinite}} < 0$), which means that kaolinite precipitation dominates the kaolinite dissolution. However, averaging the concentrations over the whole network (or even over the reactive pores) predicts kaolinite dissolution to be dominant. Averaging the reaction rate over the network predicts kaolinite precipitation at early injection time and then changes into kaolinite dissolution in the steady-state condition.

In all other cases including albite (Figure 6B.1−B.3), averaging over the reactive pores matches the surface-weighted reaction rate. For albite reactions, volume averaging over the whole network overestimates the reaction rate. Because, not only the average pH is lower in the network in comparison to the local pH of the reactive pores, but also the fluid saturation is further from equilibrium in comparison to the local fluid in the reactive pores. Moreover, the averaged reaction rates work better for less complex minerals such as quartz because, for these minerals, fewer heterogeneous parameters play a role in the calculation of the rate. To further clarify this point, one must pay attention that, in the case of albite, H_4SiO_4, $Al(OH)_4^-$, Na^+, H^+, and OH^- play a role in the rate calculation, while in the case of quartz, only the H_4SiO_4 concentration (and the subsequent dissociation reaction products) is important. An interesting point in Figure 6A.1−A.3 is that the surface-weighted kaolinite reaction rate changes from being precipitation-dominant in case 1 into dissolution-dominant in cases 2 and 3. In the cases with large reactive pores, the reactive pores are flushed faster, and the ratio of the pore-unit volume to surface area is greater than the other two cases. The residing fluid in the reactive pores does not reach equilibrium or precipitation state.

To give a better insight into the reactive transport, macroscopic dimensionless Damköhler number (Da) is estimated for the mineral i using the expression $\text{Da}_i = \frac{\mathcal{A}_i \times R_{T,i} \times L}{U \times C_{\text{eq}} \times \text{PV}_{\text{reactive}}}$, where $\mathcal{A}_i$ denotes the reactive surface of the mineral, L is the characteristic length of the system (sample

DOI: 10.1021/acsearthspacechem.9b00056
ACS Earth Space Chem. 2019, 3, 2045−2057

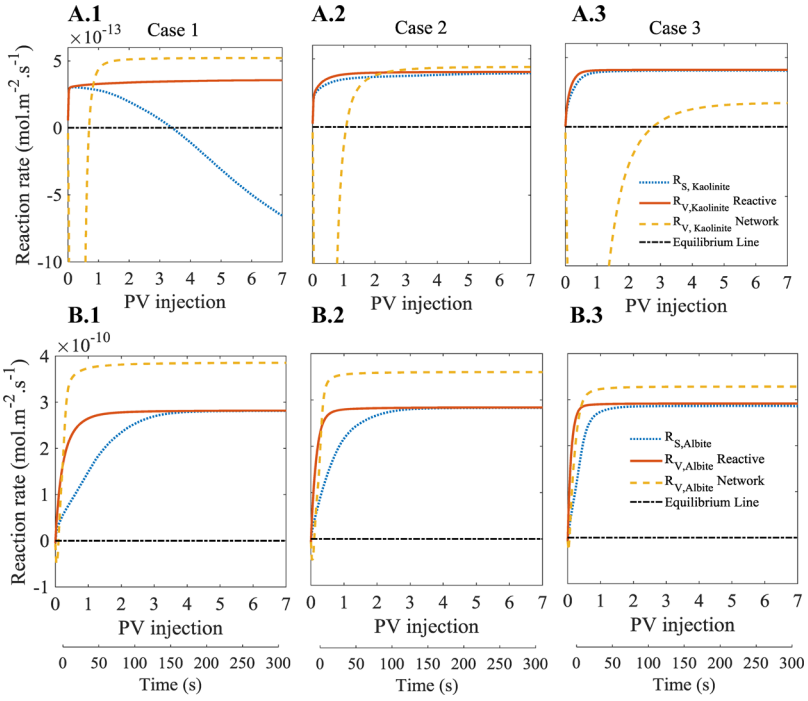

Figure 6. Effect of the spatial distribution of the reactive pores on the surface and volume-averaged reaction rates for (A.1−A.3) kaolinite and (B.1−B.3) albite minerals after 7 pore volumes of injection.

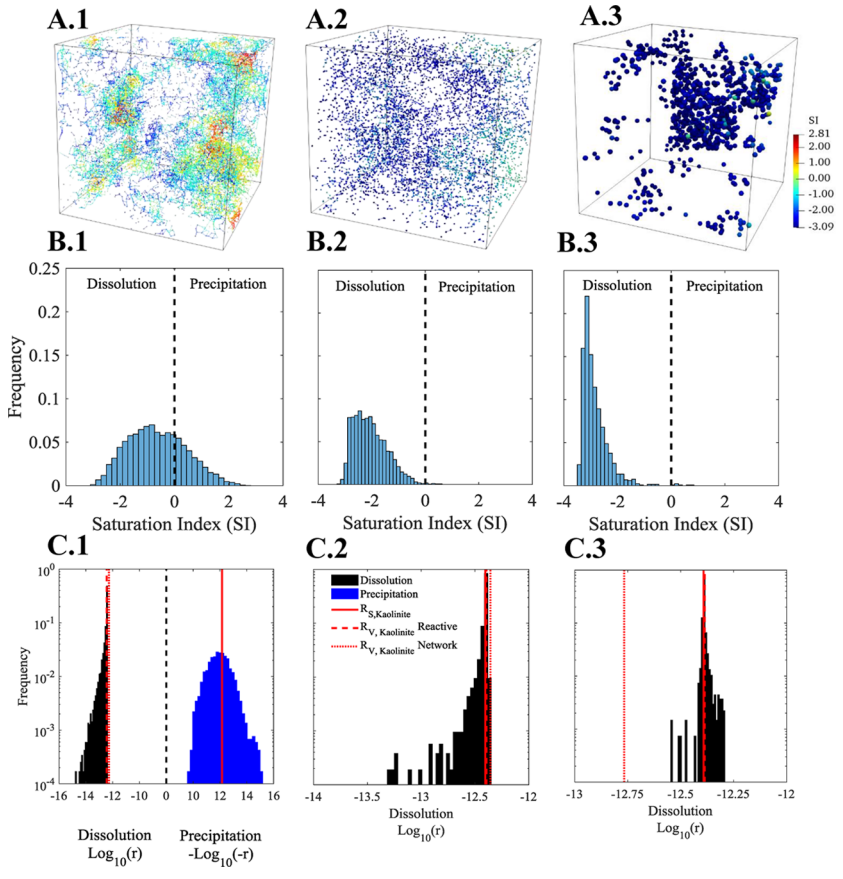

Figure 7. (A.1−A.3) Effect of the spatial distribution of the reactive pores on the dissolution/precipitation pattern of kaolinite, (B.1−B.3) distribution of the saturation index (SI) in the reactive pores (SI < 0 shows dissolution, SI > 0 shows precipitation, and equilibrium is also shown with a dashed black vertical line), and (C.1−C.3) logarithm of the reaction rate distribution in the reactive pores. (Note that pore-body sizes are scaled in the network visualizations.)

DOI: 10.1021/acsearthspacechem.9b00056
ACS Earth Space Chem. 2019, 3, 2045−2057

length), U is the injection velocity, C_{eq} is the steady-state concentration of the main element (H^+) in the reactive pores, and $PV_{reactive}$ is the volume of reactive pores. In case 1, the Damköhler number varies between 0.044 and 1500 for kaolinite and siderite, respectively. As $Da_{siderite} \gg 1$, which is the most reactive mineral, it can be concluded that the local equilibrium approach (LEA) can be followed for this mineral.[63] It it noteworthy to mention that, in this case, Da_{albite} = 17.8 and $Da_{anorthite}$ = 136.9. It is also interesting that Da will decrease from case 1 to case 3. Even though the average pH in the reactive pores decreases, the reactive surface corresponds to a higher ratio of sample pore volume since the reactive pores are larger in case 3.

Figure 7 presents the dissolution/precipitation pattern of kaolinite in the network (Figure 7A.1−A.3) and distribution of the saturation index in the reactive pores. Figure 7A.1 shows that precipitation takes place in the middle of the reactive clusters and mostly in the downstream half of the sample because, in these regions, the fluid becomes saturated with respect to the species. Also, precipitation of the minerals is not seen in the isolated reactive pores or small clusters because, in these regions, the saturation index is mostly affected by the adjacent pores and the fluid becomes diluted. In Figure 7B.1−B.3, the distribution histogram is shifted to the left-hand side of the equilibrium line as the reactive pores are moved from the small pores to the larger pores. Based on the provided results, case 1 is more challenging in terms of geochemical modeling due to the separation of pores contributing to flow from the pores contributing to geochemistry. This implies a zonation in the reactive transport that can give insights into the geochemical modeling at the Darcy scale.

Effect of Hydrodynamic Conditions. Since the system dynamics plays an important role in reactive transport, in this section, the effects of the flow rate on the pore-scale heterogeneities in the reactive transport and continuum-scale reaction rates are discussed. For this purpose, the network with 23.5% of the smallest pores being reactive (case 1) is chosen. We expect the clay minerals to be more abundant in the small pores of the sandstone rocks because they play a role as pore-filling and pore-bridging minerals.[62,64−66] It was also shown in the previous sections that upscaling of geochemical reactions of this system is more challenging. To study the effect of flow rate, three simulation cases are designed: the first one (case 4) has the average velocity of 3.66×10^{-3} cm/s; the second simulation (case 5) has the flow velocity of 1.26×10^{-2} cm/s, which is identical to case 1; and also, the last simulation (case 6) has the average pore velocity of 7.33×10^{-2} cm/s (a summary of simulation cases is presented in Table S-4). These pore velocities correspond to the pressure gradients of 15.2, 54.3, and 304.3 kPa/m, respectively. Figure 8A,B presents the transient behavior of average pH and aluminum concentration in both reactive pores and the whole network. Generally, increasing the flow rate results in a decrease in the average pH of the network and the reactive pores but results in a lower aluminum concentration. This is because, when the flow rate is increased, the pores are flushed faster with the injection fluid, and the chemical reactions do not have enough resident time to proceed due to a lower Damköhler number.

Figure 9 depicts the steady-state distribution of pH and logarithm of the total aluminum concentration for the whole network. As shown in Figure 9A.2, the frequency of the lower pH (around 5−5.5) is higher than that of Figure 9A.1, which corresponds to a lower injection flow rate. In the case of

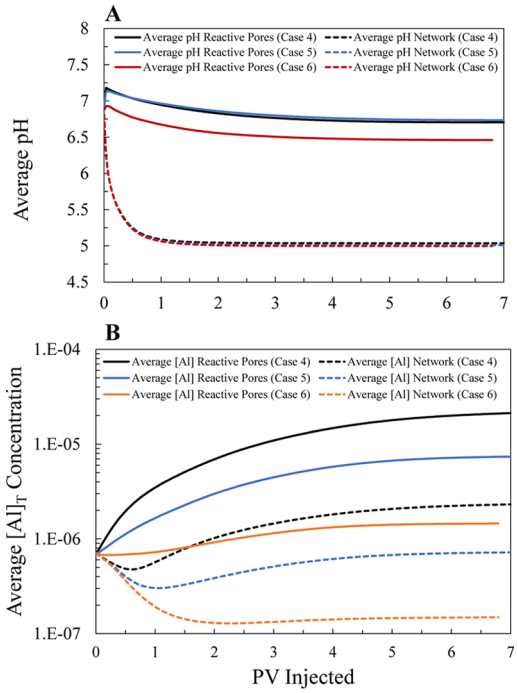

Figure 8. Effect of the injection flow rate on (A) the transient behavior of the average pH and (B) the average aluminum concentration of the network and the reactive pores. (Injection flow rates are equal to 0.41, 1.41, and 8.2 PV/min for cases 4, 5, and 6, respectively. Injection water pH and aluminum concentration are 4.9 and 1.8×10^{-8} m, respectively.)

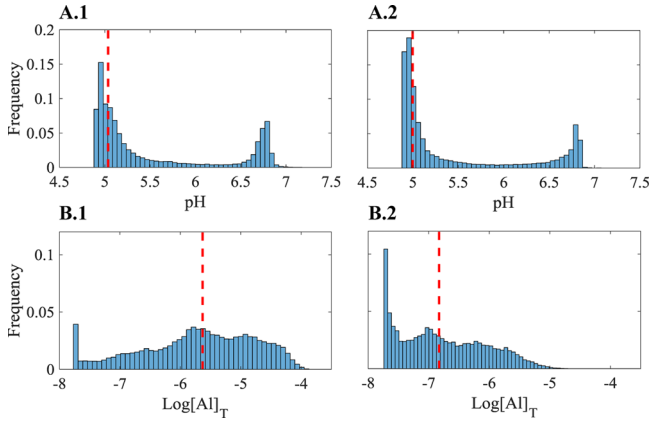

Figure 9. Distribution of pH and logarithm of the total aluminum concentration (log $[Al]_T$) in the network for (A.1, B.1) case 4 and (A.2, B.2) case 6. In each case, the average value is shown with a vertical red dashed line.

aluminum concentration, for case 4, the concentration profile spans up to 4 orders of magnitude, while for case 6, the span is almost 3 orders of magnitude. Additionally, the aluminum concentration distribution is shifted to lower values as the flow rate increases. Both phenomena can be explained by the decrease in the Damköhler number at higher injection flow rates. As the Damköhler number decreases, the geochemical reactions take place slower in comparison to transport, and consequently, the steady-state H^+ concentration increases. Conversely, the aluminum concentration decreases in the system as aluminum is a product of the geochemical reactions, and therefore, both of these effects result in higher steady-state solid-phase reaction rates.

DOI: 10.1021/acsearthspacechem.9b00056
ACS Earth Space Chem. 2019, 3, 2045−2057

Figure 10 illustrates the effect of the injection flow rate on the surface-weighted and volume-averaged reaction rates of

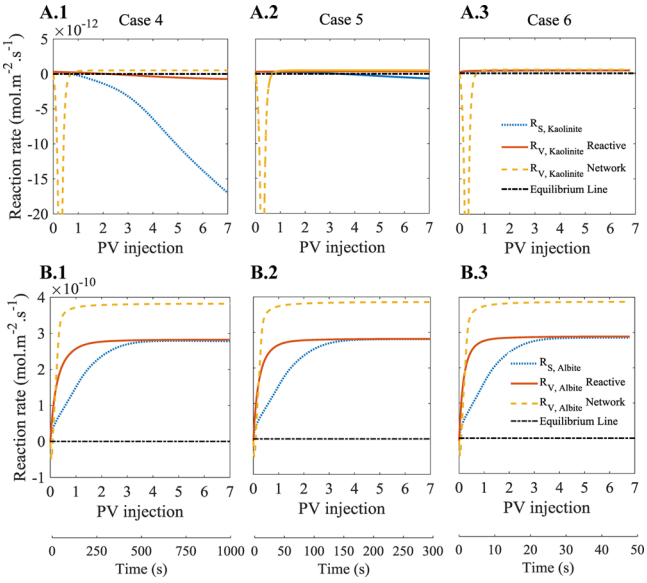

Figure 10. Effect of injection velocity on surface-weighted (R_S) and volume-weighted (R_V) averaged reaction rates for (A.1−A.3) kaolinite and (B.1−B.3) albite minerals.

kaolinite (Figure 10A.1−A.3) and albite (Figure 10B.1−B.3). As the injection velocity increases, the reaction rate usually increases because of two factors: first, the reactions are further from equilibrium condition because the system is flushed faster, and second, the local and average pH values are lower (more acidic), which result in a higher reaction rate. For kaolinite, the direction of the reaction is highly dependent on the injection flow rate; at low flow rates, the reactions are closer to equilibrium and precipitation (SI $\geq$ 0). Consequently, in case 4, a high precipitation rate of kaolinite is seen. Conversely, in case 6, the kaolinite dissolution reaction dominates. In all cases, the averaged kaolinite reaction rate over the network predicts dissolution, which is wrong even in the prediction of the reaction direction for cases 4 and 5. The averaged reaction rate over reactive pores predicts the kaolinite reaction direction correctly in case 4 but underestimates the reaction rate. In case 5, the direction of the reaction is predicted incorrectly, and finally, averaging over the system provides an acceptable estimation of surface-weighted averaged reaction rate in case 6 in comparison to cases 4 and 5.

To clarify the sensitivity of the kaolinite reaction rate to the injection flow rate, the steady-state saturation index distributions of the reactive pores are presented for cases 4−6 in Figure 11. As the injection flow rate increases, the saturation index (SI) distribution is shifted to the left-hand side of the equilibrium line, implying a reduction in the saturation index of kaolinite (lower chance of precipitation).

Effect of Network Structure. In this section, the effect of the network structure on the multicomponent reactive transport in porous media is studied. For this purpose, different scenarios, with different Péclet numbers, are simulated on two different networks, an uncorrelated (random) network and a network with a correlation length of 20 μm (see Figure 1). In all simulations, 23.5% of the smallest pore units are reactive, and the other pores are nonreactive. The macroscopic Péclet number is

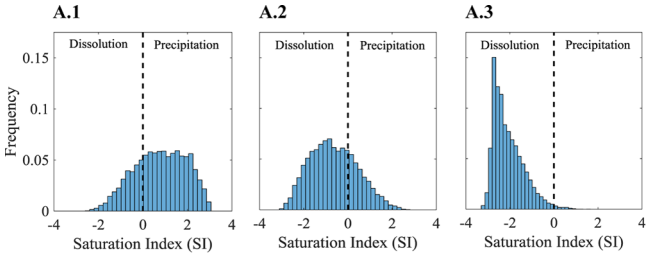

Figure 11. (A.1−A.3) Steady-state distribution of kaolinite saturation index (SI) in the reactive pores for cases 4−6.

calculated as $\langle Pe \rangle = \frac{Lu}{D}$, where L (mm) is the sample length, u (mm/s) is the flow velocity, and D (mm^2/s) is the diffusion coefficient. We have calculated the Péclet number with respect to the H^+ diffusion coefficient since the availability of the H^+ ion is important for the kinetic reactions. The H^+ ion has a very small size and is the fastest ion among the existing species in this study. The Péclet number can be up to 1 order of magnitude larger for slower species. In all cases, 7 pore volumes of water is injected. The results of the steady-state conditions are plotted for different Péclet numbers to draw a comparison on the effect of the network structure on the pore-scale conductive-diffusive reactive transport properties.

Figure 12 presents the average pH for the reactive pores and the network for both random and correlated networks for

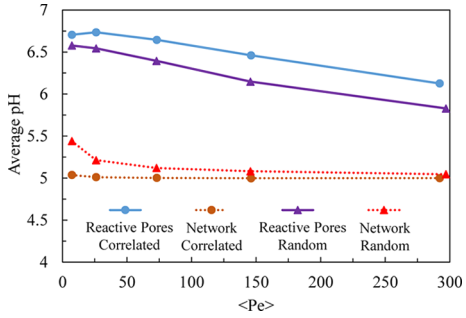

Figure 12. Average pH in the reactive pores and the whole network for the correlated and uncorrelated (random) networks at different Péclet numbers. (Note that injection water pH is 4.9.)

different Péclet numbers. Generally, the pH decreases with increasing Péclet number as the influx of H^+ ion is larger. However, the change is more significant in the reactive pores as the network average pH is mostly controlled by the nonreactive pores.

Figure 13A illustrates the effect of Péclet number on the reaction rate in both random and correlated networks. It has been shown that kaolinite precipitation is likely to happen in low Péclet numbers. At high Péclet numbers, the increasing injection rate results in a larger dissolution rate. An interesting point in Figure 13A is that, at small Péclet numbers in the correlated network, kaolinite precipitation outweighs dissolution, and the overall reaction rate is negative. Conversely, averaging over the network (network-averaged reaction rate) predicts kaolinite dissolution, while the results are opposite in the random network. Also, averaging over the network in large Péclet numbers overestimates the dissolution rate.

Figures 13B,C show the steady-state reaction rates for albite and siderite, respectively. The reaction rate is larger in the uncorrelated (random) network because the reactive pores do

DOI: 10.1021/acsearthspacechem.9b00056
ACS Earth Space Chem. 2019, 3, 2045−2057

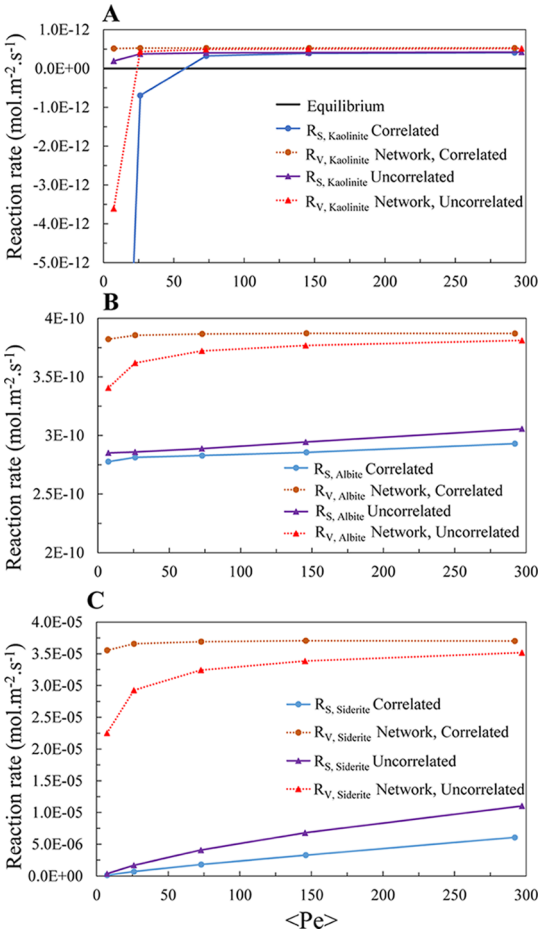

Figure 13. Surface-weighted averaged (R_S) and network-averaged (R_V network) reaction rates for (A) kaolinite, (B) albite, and (C) siderite in the correlated and uncorrelated (random) networks.

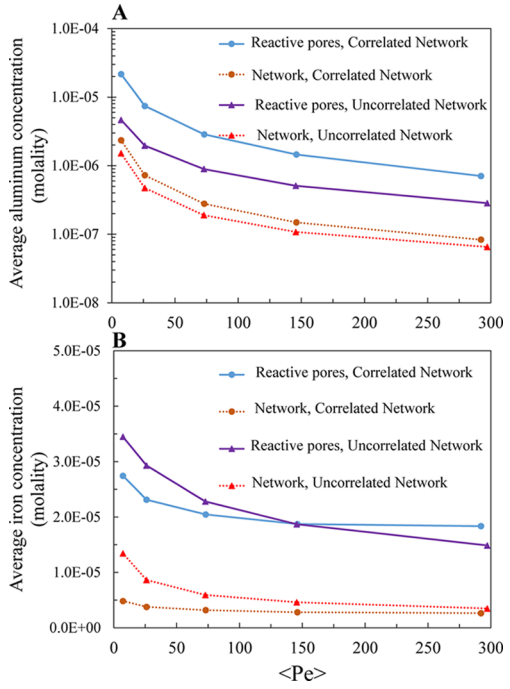

Figure 14. (A) Average aluminum concentration and (B) average iron concentration for reactive pores and network for both correlated and uncorrelated (random) networks in different Péclet numbers. (Note that injection water aluminum and iron concentrations are 1.8×10^{-8} and 1.7×10^{-8} m, respectively.)

not make clusters and are dispersed in the network. In the correlated network, they form reactive clusters. In both cases, averaged reaction rates over the network overestimate the surface-weighted average reaction rate because of the pore-scale heterogeneity in pH and species concentration distribution in the network.

It appears from Figure 13B,C that the difference between the network-averaged and surface-weighted averaged reaction rates is smaller for the case with the uncorrelated (random) structure. This increases by increasing the Péclet number. In the uncorrelated (random) network, the reactive pores are connected to the nonreactive pores, so the system is less heterogeneous with respect to the reactive transport properties in comparison to the correlated network. Also, at small Péclet numbers, the ion exchange between reactive and nonreactive pores is increased because diffusion becomes more important in comparison to advection, so the system is less heterogeneous.

Figure 14A,B shows the change of aluminum and iron content of the whole network and the reactive pores for both random and correlated networks with different Péclet numbers. Generally, the concentration decreases with increasing Péclet number as the system is flushed with a higher flow rate. The effect is more pronounced in the case of the reactive pores averaged as the reaction takes place in the reactive pores.

SUMMARY AND CONCLUSIONS

In this work, a geochemistry module, PhreeqcRM, is coupled with an irregular lattice pore-network model consisting of 56,000 pores, representative of sandstone rock samples. Correlated (correlation length = 20 μm) and uncorrelated (random) networks were generated with the same pore size distribution and topology. In this research, 5 kinetic solid-phase reactions along with 14 equilibrium aqueous reactions were solved in reactive pores using the sequential noniterative approach (SNIA) to simulate high-temperature, steady-state single-phase reactive flow, relevant to aquifer thermal energy storage (ATES) and geothermal energy extraction schemes.

Five different minerals, consisting of quartz, kaolinite, albite, anorthite, and siderite, were considered in the network to represent a realistic sandstone mineral assemblage. We have calculated three different average reaction rates to quantify the associated error with upscaling and averaging reaction rates in porous media: surface-weighted averaged (R_S) and volume-averaged reaction rates in reactive pores (R_V reactive) and in the network (R_V network).

The effects of spatial distribution of the reactive pores, injection velocity, and network structure (correlated and random cases) were studied on different characteristics of the reactive transport in porous media. To be consistent with the existing characteristics of sandstone in the nature, we chose the location of the reactive pore with respect to their sizes and generated different cross-correlated networks, while the total reactive surface area was conserved.

The following major concolusions can be made based on the performed simulations:

1. Simulation results show that spatial distribution of the reactive pores has a strong effect on the reactive transport in porous media. In the case in which the smallest pores

DOI: 10.1021/acsearthspacechem.9b00056
ACS Earth Space Chem. 2019, 3, 2045−2057

are reactive, the fluid is likely to become supersaturated, so kaolinite precipitation is likely to happen. The reasons are low local flux and reactive cluster formation in the correlated network. Also, the average pH of the system is higher in comparison to the cases in which the middle-sized pores or the largest pores are reactive.

2. Averaging the reaction rates through both network and reactive pores overestimates the surface-weighted reaction rates, while for the kaolinite, it cannot even determine the dominant reaction direction. For the simulation case in which the smallest pores are reactive, precipitation dominates the kaolinite dissolution, while the averaged kaolinite reaction rates predict kaolinite dissolution to be the dominant mechanism.
3. Kaolinite precipitation is more likely to happen in low flow rates. It is worth noting that, in low flow rates, the geochemistry becomes more heterogeneous, and distribution profiles for concentrations of different species cover a broader range. In the case of a high flow rate, the system is flushed faster with fresh water, and the geochemical reactions have less time to proceed. It can be concluded that formation damage due to the geochemical reactions is more likely to happen in low injection rates. So, it can be avoided by increasing the flow rate higher than the critical flow rate, in which the kaolinite precipitation is not dominant in comparison to dissolution.
4. Correlation length has a significant effect on the reactive transport in porous media. In the random network, the concentration of the reactive pores is affected by neighboring pores, which leads to less chance of mineral precipitation. In such a network, flow fingering is less likely to happen, so the system becomes more homogeneous compared to the correlated case. So, because of a lower extent of pore-scale heterogeneity, the error of the averaged reaction rates is smaller in comparison to the correlated network with the same specifications.
5. In a random network, as the reactive clusters are less likely to happen, the geochemical reaction rates are faster due to a lower local pH in the reactive pores as well as a lower saturation index due to mass transfer with the nonreactive pores and the higher local flux in comparison to the correlated network.

■ ASSOCIATED CONTENT

Supporting Information

The Supporting Information is available free of charge on the ACS Publications website at DOI: 10.1021/acsearthspacechem.9b00056.

Fundamental description of the following topics and further information on simulation sections: supporting theoretical background, reaction equilibrium constant, and diffusion coefficients; calculation flowchart for the coupled PNM-geochemistry model; solid- and aqueous-phase geochemical reactions and rate constants; and summary table of simulation cases (PDF)

■ AUTHOR INFORMATION

Corresponding Author

*E-mail: Vahid.niasar@manchester.ac.uk.

ORCID

Vahid Joekar-Niasar: 0000-0002-9472-555X

Rouhi Farajzadeh: 0000-0003-3497-0526

Notes

The authors declare no competing financial interest.

Datasets related to this article can be found at DOI: 10.17632/gr6mrgn2z6.2, an open-source online data repository hosted at Mendeley Data.

■ ACKNOWLEDGMENTS

We acknowledge the University of Manchester for providing the Ph.D. funding for H.E. through President's Doctoral Scholarship (PDS).

■ NOMENCLATURE

a	surface area (m^2)
D	diffusion coefficient ($m^2\ s^{-1}$)
E_a	activation energy (kJ mol^{-1})
ΔH^0	standard enthalpy of reaction (kJ mol^{-1})
K_{eq}	equilibrium constant
k	reaction rate constant
k_H	acid mechanism rate constant
K_{H_2O}	neutral mechanism rate constant
K_{OH}	base mechanism rate constant
m	dependence of rate on saturation state constant
n_s	degree of rate dependence constant
P	pressure (Pa)
Q	flow rate (m^3/s)
R	universal gas constant (kJ $mol^{-1}\ K^{-1}$)
r	reaction rate ($mol/m^2\ s$)
R_S	surface-weighted reaction rate ($mol/m^2\ s$)
S	sink/source term due to geochemical interactions
R_V	volumetric-averaged (continuum scale) reaction rate ($mol/m^2\ s$)
T	absolute temperature (K)
V	pore-unit volume (m^3)

Abbreviations

ATES	aquifer thermal energy storage
IAP	ionic activity product
MICP	microbial-induced calcium carbonate precipitation
LEA	local equilibrium approach
np	number of pores
SI	saturation index

Notations

{}	species activity
[]	concentration (molality)
−	average
$\mathcal{A}$	reactive surface (m^2)
l	length (m)

Greek Letters

Ω	saturation ratio
μ	viscosity (Pa s)

■ REFERENCES

(1) Farajzadeh, R.; Matsuura, T.; van Batenburg, D.; Dijk, H. Detailed modeling of the alkali/surfactant/polymer (ASP) process by coupling a multipurpose reservoir simulator to the chemistry package PHREEQC. *SPE Reservoir Eval. Eng.* **2012**, *15*, 423−435.

(2) Kazempour, M.; Alvarado, V. Geochemically based modeling of pH-sensitive polymer injection in Berea sandstone. *Energy Fuels* **2011**, *25*, 4024−4035.

(3) Mahani, H.; Menezes, R.; Berg, S.; Fadili, A.; Nasralla, R.; Voskov, D.; Joekar-Niasar, V. Insights into the impact of temperature on the wettability alteration by low salinity in carbonate rocks. *Energy Fuels* **2017**, *31*, 7839−7853.
(4) Joekar-Niasar, V.; Mahani, H. Nonmonotonic pressure field induced by ionic diffusion in charged thin films. *Ind. Eng. Chem. Res.* **2016**, *55*, 6227−6235.
(5) Mahani, H.; Berg, S.; Ilic, D.; Bartels, W.-B.; Joekar-Niasar, V. Kinetics of Low-Salinity-Flooding effect. *SPE J.* **2015**, *20*, 8−20.
(6) Aziz, R.; Joekar-Niasar, V.; Martinez-Ferrer, P. Pore-scale insights into transport and mixing in steady-state two-phase flow in porous media. *Int. J. Multiphase Flow* **2018**, *109*, 51−62.
(7) Farajzadeh, R.; Guo, H.; van Winden, J.; Bruining, J. Cation exchange in the presence of oil in porous media. *ACS Earth Space Chem.* **2017**, *1*, 101−112.
(8) Olayiwola, S. O.; Dejam, M. A comprehensive review on interaction of nanoparticles with low salinity water and surfactant for enhanced oil recovery in sandstone and carbonate reservoirs. *Fuel* **2019**, *241*, 1045−1057.
(9) Erfani Gahrooei, H. R.; Ghazanfari, M. H.; Karimi Malekabadi, F. Wettability alteration of reservoir rocks to gas wetting condition: A comparative study. *Can. J. Chem. Eng.* **2018**, *96*, 997−1004.
(10) Joonaki, E.; Gahrooei, H. R. E.; Ghanaatian, S. Experimental study on adsorption and wettability alteration aspects of a new chemical using for enhanced oil recovery in carbonate oil reservoirs. *J. Unconv. Oil Gas Resour.* **2016**, *15*, 11−21.
(11) Johnson, J. W.; Nitao, J. J.; Knauss, K. G. Reactive transport modelling of CO_2 storage in saline aquifers to elucidate fundamental processes, trapping mechanisms and sequestration partitioning. *Geol. Soc., London, Spec. Publ.* **2004**, *233*, 107−128.
(12) Hassanpouryouzband, A.; Yang, J.; Tohidi, B.; Chuvilin, E.; Istomin, V.; Bukhanov, B.; Cheremisin, A. CO_2 capture by injection of flue gas or CO_2−N_2Mixtures into hydrate reservoirs: dependence of CO_2 capture efficiency on gas hydrate reservoir conditions. *Environ. Sci. Technol.* **2018**, *52*, 4324−4330.
(13) Babaei, M.; Islam, A. Convective-reactive CO_2 dissolution in aquifers with mass transfer with immobile water. *Water Resour. Res.* **2018**, *54*, 9585−9604.
(14) Deng, H.; Steefel, C.; Molins, S.; DePaolo, D. Fracture evolution in multimineral systems: The role of mineral composition, flow rate, and fracture aperture heterogeneity. *ACS Earth Space Chem.* **2018**, *2*, 112−124.
(15) Dejam, M.; Hassanzadeh, H. Diffusive leakage of brine from aquifers during CO2 geological storage. *Adv. Water Resour.* **2018**, *111*, 36−57.
(16) Cardoso, S. S. S.; Andres, J. T. H. Geochemistry of silicate-rich rocks can curtail spreading of carbon dioxide in subsurface aquifers. *Nat. Commun.* **2014**, *5*, 5743.
(17) Kang, Q.; Lichtner, P. C.; Viswanathan, H. S.; Abdel-Fattah, A. I. Pore scale modeling of reactive transport involved in geologic CO2 sequestration. *Transp. Porous Media* **2010**, *82*, 197−213.
(18) Hassanzadeh, H.; Pooladi-Darvish, M.; Keith, D. W. Accelerating CO_2 Dissolution in saline aquifers for geological storage - mechanistic and sensitivity studies. *Energy Fuels* **2009**, *23*, 3328−3336.
(19) Fleuchaus, P.; Godschalk, B.; Stober, I.; Blum, P. Worldwide application of aquifer thermal energy storage−A review. *Renewable Sustainable Energy Rev.* **2018**, *94*, 861−876.
(20) Brusseau, M. L. Transport of reactive contaminants in heterogeneous porous media. *Rev. Geophys.* **1994**, *32*, 285−313.
(21) Wissmeier, L.; Barry, D. A. Reactive transport in unsaturated soil: Comprehensive modelling of the dynamic spatial and temporal mass balance of water and chemical components. *Adv. Water Resour.* **2008**, *31*, 858−875.
(22) Dejam, M.; Hassanzadeh, H.; Chen, Z. Shear dispersion in a fracture with porous walls. *Adv. Water Resour.* **2014**, *74*, 14−25.
(23) Spycher, N. F.; Sonnenthal, E. L.; Apps, J. A. Fluid flow and reactive transport around potential nuclear waste emplacement tunnels at Yucca Mountain, Nevada. *J. Contam. Hydrol.* **2003**, *62-63*, 653−673.
(24) Charlet, L.; Alt-Epping, P.; Wersin, P.; Gilbert, B. Diffusive transport and reaction in clay rocks: A storage (nuclear waste, CO2, H2), energy (shale gas) and water quality issue. *Adv. Water Resour.* **2017**, *106*, 39−59.
(25) Wood, B. D.; Radakovich, K.; Golfier, F. Effective reaction at a fluid−solid interface: applications to biotransformation in porous media. *Adv. Water Resour.* **2007**, *30*, 1630−1647.
(26) Swoboda-Colberg, N. G.; Drever, J. I. Mineral dissolution rates in plot-scale field and laboratory experiments. *Chem. Geol.* **1993**, *105*, 51−69.
(27) Noiriel, C.; Oursin, M.; Saldi, G.; Haberthür, D. Direct determination of dissolution rates at crystal surfaces using 3D X-ray microtomography. *ACS Earth Space Chem.* **2019**, *3*, 100−108.
(28) Palandri, J. L.; Kharaka, Y. K. *A compilation of rate parameters of water-mineral interaction kinetics for application to geochemical modeling*; U.S. Geological Survey, 2004.
(29) Folk, R. L. *Petrology of sedimentary rocks*; Hemphill Publishing Company: 1980.
(30) Cantucci, B.; Montegrossi, G.; Vaselli, O.; Tassi, F.; Quattrocchi, F.; Perkins, E. H. Geochemical modeling of CO_2 storage in deep reservoirs: The Weyburn Project (Canada) case study. *Chem. Geol.* **2009**, *265*, 181−197.
(31) Langmuir, D. *Aqueous Environmental Geochemistry*; Prentice-Hall, Inc.: Englewood Cliffs, 601, 1997.
(32) Nogues, J. P.; Fitts, J. P.; Celia, M. A.; Peters, C. A. Permeability evolution due to dissolution and precipitation of carbonates using reactive transport modeling in pore networks. *Water Resour. Res.* **2013**, *49*, 6006−6021.
(33) Mehmani, Y.; Sun, T.; Balhoff, M. T.; Eichhubl, P.; Bryant, S. Multiblock pore-scale modeling and upscaling of reactive transport: application to carbon sequestration. *Transp. Porous Media* **2012**, *95*, 305−326.
(34) Varloteaux, C.; Vu, M. T.; Békri, S.; Adler, P. M. Reactive transport in porous media: pore-network model approach compared to pore-scale model. *Phys. Rev. E* **2013**, *87*, No. 023010.
(35) Kang, Q.; Lichtner, P. C.; Zhang, D. Lattice Boltzmann pore-scale model for multicomponent reactive transport in porous media. *J. Geophys. Res.: Solid Earth* **2006**, *111*, B05203.
(36) Patel, R. A.; Perko, J.; Jacques, D.; De Schutter, G.; Van Breugel, K.; Ye, G. A versatile pore-scale multicomponent reactive transport approach based on lattice Boltzmann method: Application to portlandite dissolution. *Phy. Chem. Earth, Parts A/B/C* **2014**, *70-71*, 127−137.
(37) Liu, M.; Mostaghimi, P. *Coupling lattice Boltzmann and finite volume methods for simulation of reactive transport*; International Symposium of the Society of Core Analysts: Colorado, USA, 2016.
(38) Maes, J.; Geiger, S. Direct pore-scale reactive transport modelling of dynamic wettability changes induced by surface complexation. *Adv. Water Resour.* **2018**, *111*, 6−19.
(39) Gray, F.; Anabaraonye, B.; Shah, S.; Boek, E.; Crawshaw, J. Chemical mechanisms of dissolution of calcite by HCl in porous media: Simulations and experiment. *Adv. Water Resour.* **2018**, *121*, 369−387.
(40) Dejam, M. Advective-diffusive-reactive solute transport due to non-newtonian fluid flows in a fracture surrounded by a tight porous medium. *Int. J. Heat Mass Transfer* **2019**, *128*, 1307−1321.
(41) Békri, S.; Thovert, J. F.; Adler, P. M. Dissolution of porous media. *Chem. Eng. Sci.* **1995**, *50*, 2765−2791.
(42) Oostrom, M.; et al. Pore-scale and continuum simulations of solute transport micromodel benchmark experiments. *Comput. Geosci.* **2016**, *20*, 857−879.
(43) Li, L.; Peters, C. A.; Celia, M. A. Upscaling geochemical reaction rates using pore-scale network modeling. *Adv. Water Resour.* **2006**, *29*, 1351−1370.
(44) Li, L.; Peters, C. A.; Celia, M. A. Effects of mineral spatial distribution on reaction rates in porous media. *Water Resour. Res.* **2007**, *43*, W01419.
(45) Li, L.; Peters, C. A.; Celia, M. A. Applicability of averaged concentrations in determining geochemical reaction rates in heterogeneous porous media. *Am. J. Sci.* **2007**, *307*, 1146−1166.

DOI: 10.1021/acsearthspacechem.9b00056
ACS Earth Space Chem. 2019, 3, 2045−2057

(46) Ameri, A.; Raoof, A.; Blonk, C.; Cnudde, V. Detailed modeling of carbonate acidizing by coupling a multi-purpose pore-network simulator to the chemistry package PHREEQC-application to chelating agents. In *SPE Latin America and Caribbean Petroleum Engineering Conference*; Society of Petroleum Engineers, 2017.
(47) Qin, C.-Z.; Hassanizadeh, S. M.; Ebigbo, A. Pore-scale network modeling of microbially induced calcium carbonate precipitation: Insight into scale dependence of biogeochemical reaction rates. *Water Resour. Res.* **2016**, *52*, 8794−8810.
(48) Al-Khulaifi, Y.; Lin, Q.; Blunt, M. J.; Bijeljic, B. Reaction rates in chemically heterogeneous rock: Coupled impact of structure and flow properties studied by X-ray microtomography. *Environ. Sci. Technol.* **2017**, *51*, 4108−4116.
(49) Holmslykke, H. D.; Kjøller, C.; Fabricius, I. L. Core flooding experiments and reactive transport modeling of seasonal heat storage in the hot deep gassum sandstone formation. *ACS Earth Space Chem.* **2017**, *1*, 251−260.
(50) Parkhurst, D. L.; Appelo, C. *Description of input and examples for PHREEQC version3: a computer program for speciation, batch-reaction, one-dimensional transport, and inverse geochemical calculations*; U.S. Geological Survey: 2013.
(51) Charlton, S. R.; Parkhurst, D. L. Modules based on the geochemical model PHREEQC for use in scripting and programming languages. *Comput. Geosci.* **2011**, *37*, 1653−1663.
(52) Parkhurst, D. L.; Wissmeier, L. PhreeqcRM: A reaction module for transport simulators based on the geochemical model PHREEQC. *Adv. Water Resour.* **2015**, *83*, 176−189.
(53) Bonte, M.; van Breukelen, B. M.; Stuyfzand, P. J. Temperature-induced impacts on groundwater quality and arsenic mobility in anoxic aquifer sediments used for both drinking water and shallow geothermal energy production. *Water Res.* **2013**, *47*, 5088−5100.
(54) Steefel, C.; DePaolo, D.; Lichtner, P. Reactive transport modeling: An essential tool and a new research approach for the earth sciences. *Earth Planet. Sci. Lett.* **2005**, *240*, 539−558.
(55) Bozau, E.; Häußler, S.; van Berk, W. Hydrogeochemical modelling of corrosion effects and barite scaling in deep geothermal wells of the North German Basin using PHREEQC and PHAST. *Geothermics* **2015**, *53*, 540−547.
(56) Joekar-Niasar, V.; Hassanizadeh, S. M.; Leijnse, A. Insights into the relationships among capillary pressure, saturation, interfacial area and relative permeability using porenetwork modeling. *Transp. Porous Media* **2008**, *74*, 201−219.
(57) Leng, C. C. The effect of spatial correlation on viscous fingering in a dynamic porenetwork model with Delaunay tessellated structure. M.Sc. thesis, 2013.
(58) Babaei, M.; Joekar-Niasar, V. A transport phase diagram for pore-level correlated porous media. *Adv. Water Resour.* **2016**, *92*, 23−29.
(59) Kanney, J. F.; Miller, C. T.; Kelley, C. T. Convergence of iterative split-operator approaches for approximating nonlinear reactive transport problems. *Adv. Water Resour.* **2003**, *26*, 247−261.
(60) Barry, D. A.; Bajracharya, K.; Crapper, M.; Prommer, H.; Cunningham, C. J. Comparison of split-operator methods for solving coupled chemical non-equilibrium reaction/groundwater transport models. *Math. Comput. Simul.* **2000**, *53*, 113−127.
(61) Carrayrou, J.; Mosé, R.; Behra, P. Operator-splitting procedures for reactive transport and comparison of mass balance errors. *J. Contam. Hydrol.* **2004**, *68*, 239−268.
(62) Gao, J.; Xing, H.; Tian, Z.; Pearce, J. K.; Sedek, M.; Golding, S. D.; Rudolph, V. Reactive transport in porous media for CO2 sequestration: Pore scale modeling using the lattice Boltzmann method. *Comput. Geosci.* **2017**, *98*, 9−20.
(63) Nasralla, R. A.; Snippe, J. R.; Farajzadeh, R. Coupled geochemical-reservoir model to understand the interaction between low salinity brines and carbonate rock. *SPE Asia Pacific Enhanced Oil Recovery Conference*; Society of Petroleum Engineers: 2015.
(64) Krohn, C. E. Sandstone fractal and euclidean pore volume distributions. *J. Geophys. Res.: Solid Earth* **1988**, *93*, 3286−3296.
(65) Long, H.; Swennen, R.; Foubert, A.; Dierick, M.; Jacobs, P. 3D quantification of mineral components and porosity distribution in Westphalian C sandstone by microfocus X-ray computed tomography. *Sediment. Geol.* **2009**, *220*, 116−125.
(66) Lai, P.; Moulton, K.; Krevor, S. Pore-scale heterogeneity in the mineral distribution and reactive surface area of porous rocks. *Chem. Geol.* **2015**, *411*, 260−273.

DOI: 10.1021/acsearthspacechem.9b00056
ACS Earth Space Chem. 2019, 3, 2045−2057